Anisotropic three-dimensional quantum Hall effect in topological nodal-line semimetals

Mingqi Chang [1,*] and Rong Ma [2,†]

[1] *Interdisciplinary Center for Fundamental and Frontier Sciences, Nanjing University of Science and Technology, Jiangyin, Jiangsu 214443, China*

[2] *Jiangsu Key Laboratory for Optoelectronic Detection of Atmosphere and Ocean, Nanjing University of Information Science and Technology, Nanjing 210044, China*

(Received 7 December 2023; revised 6 April 2024; accepted 25 June 2024; published 8 July 2024)

The three-dimensional (3D) quantum Hall effect (QHE) has been intensely studied in Weyl semimetals and Dirac semimetals in recent years. Here, we study the 3D QHE in nodal-line semimetal through calculating the Hall conductivity numerically in a nodal-line semimetal slab. It is found that the Hall conductivity in nodal-line semimetal is anisotropic with respect to the magnetic field, Fermi energy, and sample thickness when the magnetic field is perpendicular to or parallel to the nodal line. The Hall conductivity is symmetric with respect to the energy of the nodal line in both cases. When the Fermi energy deviates from the nodal line, a Hall plateau appears and the plateau is wider and higher for the magnetic field parallel to the nodal line than perpendicular to the nodal line. For magnetic field dependence, the Hall conductivity follows $1/B$ dependence when the magnetic field is perpendicular to the nodal line, while it is independent on the magnetic field parallel to the nodal line. Moreover, the Hall conductivity as a function of sample thickness is independent of the sample thickness for the magnetic field perpendicular to the nodal line, while it is a increasing function for the magnetic field parallel to the nodal line. We give a possible explanation for these anisotropies from the energy spectrum of Landau bands under the magnetic field. This unique anisotropic 3D QHE can be a transport feature to recognize the topological nodal-line semimetals.

DOI: 10.1103/PhysRevB.110.045413

I. INTRODUCTION

In recent years, three-dimensional (3D) quantum Hall effect (QHE) in topological semimetals has attracted great interest in condensed matter physics [1–16]. Topological semimetals are 3D phases of matter with gapless electronic structures protected by topology and symmetry. Weyl and Dirac semimetals are the famous topological semimetals, in which the low-energy excitations can be described by Weyl and Dirac equations [17–26]. In Weyl and Dirac semimetals, the conduction and valence bands touch at discrete points, which are called Weyl nodes. The surface states in Weyl and Dirac semimetals are Fermi arcs connected to the projections of the bulk nodal points. In a Weyl semimetal with two Weyl nodes, it is proposed that the Fermi arcs at opposite surfaces can support the 3D QHE through the Weyl nodes [1]. Following the theoretical prediction, this 3D QHE has been observed in Dirac semimetal Cd_3As_2 in various experiments [27–33].

For topological nodal-line semimetals, the conduction and valence bands intersect along a closed loop. The surface states form the so-called drumhead-like surface states [34,35]. The nodal-line semimetal has been proposed theoretically or confirmed experimentally in various systems, including [20], graphene networks [36], Cu_3XN family (X = Ni, Cu, Pd, Ag, Cd) [37,38], alkali earth metals [39,40], group-IV tellurides (SnTe, GeTe) [41], WHX family (W = Gd, Zr, Hf, La; H = Si, Ge, SN, Sb; X = O, S, Se, Te) [42–51], CaTX family (T = Cd, Ag; X = P, Ge, As) [52], Ta_3SiTe_6 [53], AlB_2 [54], Ca_3P_2 [35,55], and the cold atom system [56].

The transport feature of materials is one of the major approaches to study the electronic properties of topological materials. In nodal-line semimetal, the bulk states and surface states produce a number of interesting transport phenomena, such as De Haas–van Alphen quantum oscillations [42,43], anisotropic magnetoresistance [45,46], spin-resolved transport [57], weak localization and antilocalization [58], etc. In Weyl and Dirac semimetals, the 3D QHE has been studied intensely. In Weyl semimetal, the Fermi arcs in opposite surfaces form a complete Fermi loop supporting the QHE. In Dirac semimetal, the Fermi arc surface in one surface can form a complete Fermi loop, producing QHE. The drumhead-like surface states in nodal-line semimetal should also be able to host QHE. This topic has been studied using non-Hermitian bulk theory [59]. Therefore, the 3D QHE in nodal-line semimetal needs further research.

In this paper, we study the 3D QHE in nodal-line semimetals through numerically calculating the Hall conductivity of a nodal-line semimetal slab. We get the anisotropic quantized Hall conductivities which are dependent on the direction of magnetic fields. The Hall conductivities under magnetic fields along different directions show anisotropic as the function of Fermi energy, magnetic field, and the thickness of the slab. The Hall conductivity as a function of Fermi energy is symmetric with respect to $E_F = 0$. A wide plateau appears

*Contact author: changmingqi@njust.edu.cn
†Contact author: njrma@hotmail.com

when the Fermi energy deviates from $E_F = 0$. However, the plateau for the magnetic field parallel to the nodal line is higher and wider than that for the magnetic field perpendicular to the nodal line. As for the magnetic field dependence, the Hall conductivity follows the usual $1/B$ dependence for the magnetic field perpendicular to the nodal line. However, the Hall conductivity is independent of the magnetic field parallel to the nodal line. As for the thickness dependence, the Hall conductivity is independent of the thickness of the sample when the thickness is greater than a critical value for the magnetic field perpendicular to the nodal line, while the Hall conductivity is an increasing function for the magnetic field parallel to the nodal line. We give a possible explanation for these anisotropies from the energy spectrum of Landau bands under the magnetic field. This unique anisotropic 3D QHE can be a transport feature to recognize the nodal-line semimetals.

The rest of the paper is organized as follows. In Sec. II, we introduce the model Hamiltonian of a nodal-line semimetal. In Sec. III, we numerically calculate the Landau bands for $B||z$ and $B||y$. In Sec. IV, we present the Hall conductivity calculated numerically in a nodal-line semimetal slab when the magnetic field is applied. In Sec. V, we give a possible explanation for the anisotropic Hall conductivities. The final section contains a brief summary.

II. MODEL

We consider a 3D model of nodal-line semimetal [57,58,60],

$$H = Ak_z\sigma_x + M\left(k_0^2 - \mathbf{k}^2\right)\sigma_z, \tag{1}$$

where (σ_x, σ_z) are the Pauli matrices, and $\mathbf{k} = (k_x, k_y, k_z)$ is the wave vector. A, M, and k_0 are the model parameters. The energy dispersion of this model is

$$E_\pm^{\mathbf{k}} = \pm\sqrt{A^2k_z^2 + M^2\left(k_0^2 - \mathbf{k}^2\right)^2}, \tag{2}$$

with $\pm$ for the conductance and valence bands. The model has a line node defined by $k_y^2 + k_z^2 = k_0^2$ and $k_z = 0$ with the same energy $E = 0$.

The topology of this model can be obtained. Take the transverse wave vector $\mathbf{k}_{||} = (k_x, k_y)$ as a parameter. For $|\mathbf{k}_{||}| = \sqrt{k_x^2 + k_y^2} < k_0$ inside the nodal line, this model is a topological insulator with an energy gap. One can verify that the Berry phase $\gamma_B = \pi$ is nontrivial with $\gamma_B = i\int_{-\infty}^{\infty} dk_z \langle u_-(\mathbf{k})|\partial_{k_z} u_-(\mathbf{k})\rangle$. Otherwise, the model is a normal insulator with $\gamma_B = 0$ for $|\mathbf{k}_{||}| > k_0$. Therefore, for $\mathbf{k}_{||}$ inside the nodal line, the nontrival Berry phase leads to the drumhead-like surface states enclosed by the the projection of the nodal loop onto the surface at an open boundary. For $\mathbf{k}_{||}$ outside the nodal line, the model becomes a normal insulator, and no surface states show up.

In Fig. 1, we plot the energy spectrum of nodal-line semimetal in the momentum space and the drumhead-like surface states. The line node lies on the k_x-k_y plane. For the surface parallel to the k_x-k_y plane, the surface states on the boundary are enclosed by the projection of the nodal line, forming the drumhead-like surface states. For the surface perpendicular to the k_x-k_y plane, the projection of the nodal line is a straight line. The anisotropic surface states in nodal-line semimetal may lead to the anisotropic property.

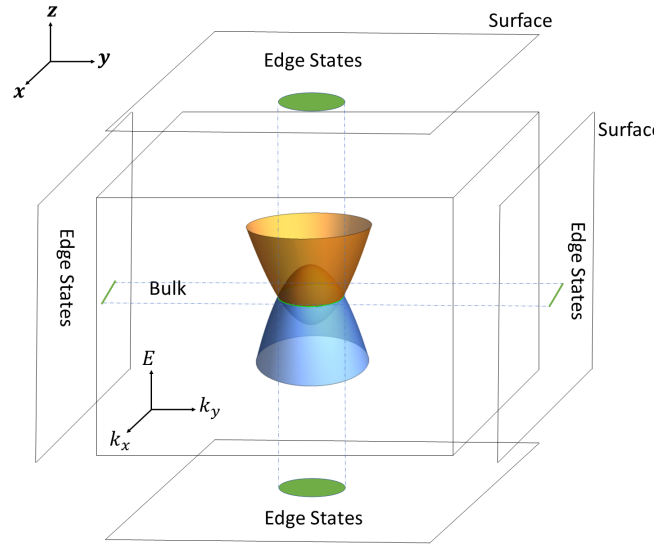

FIG. 1. The energy spectrum of the nodal-line semimetal in momentum space, and the illustration of surface states. The nodal lines are labeled as green lines. The surface states are labeled on the boundary as green surface and lines.

III. LANDAU BANDS

First, we consider the case when a magnetic field along the z direction is applied. The energy spectrum is quantized to Landau bands dispersing with k_z. The vector potential under a Landau gauge is $\mathbf{A} = (0, Bx, 0)$. Using the Pierls transformation, the wave vector is replaced by

$$\mathbf{k} = \left(k_x, k_y + \frac{x}{\ell_B^2}, k_z\right), \tag{3}$$

with $\ell_B^2 = \hbar/|eB|$. We introduce the ladder operators

$$a = \frac{\ell_B}{\sqrt{2}}\left[k_x - i\left(k_y + \frac{x}{\ell_B^2}\right)\right], \tag{4}$$

$$a^\dagger = \frac{\ell_B}{\sqrt{2}}\left[k_x + i\left(k_y + \frac{x}{\ell_B^2}\right)\right]. \tag{5}$$

With the ladder operators, the Hamiltonian Eq. (1) can be written as

$$H = \begin{bmatrix} -\omega_M\left(a^\dagger a + \frac{1}{2}\right) + M_k & Ak_z \\ Ak_z & \omega_M\left(a^\dagger a + \frac{1}{2}\right) - M_k \end{bmatrix}, \tag{6}$$

with $\omega_M = 2M/\ell_B^2$, $M_k = M(k_0^2 - k_z^2)$.

The energy bands in the magnetic field are given by

$$E_\pm(n, k_z) = \pm\sqrt{A^2k_z^2 + M^2\left[k_0^2 - \frac{2}{\ell_B^2}\left(n + \frac{1}{2}\right) - k_z^2\right]^2}, \tag{7}$$

Let us focus on the band crossing of the Landau levels. The band crossing point must occur at $k_z = 0$. Therefore, we only consider the Landau levels

$$E_\pm(n, 0) = \pm\left|Mk_0^2 - \omega_M\left(n + \frac{1}{2}\right)\right|, \tag{8}$$

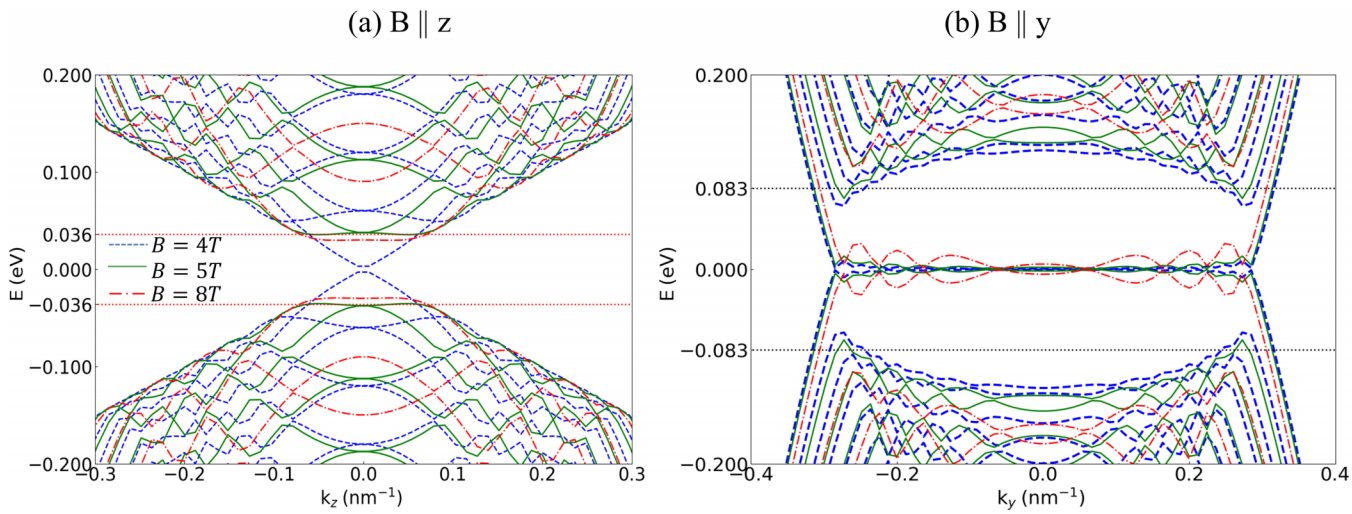

FIG. 2. The Landau level bands of a nodal-line semimetal with periodic boundary condition as a function of wave vector k_z for (a) $B||z$ and as a function of wave vector k_y for (b) $B||y$. The magnetic fields are $B = 4\ T$ (blue dashed line), $B = 5\ T$ (green solid line), and $B = 8\ T$ (red dash-dotted line). The red dotted lines in (a) are the bottom of conduction bands and the valence-band maximum. The black lines dotted in (b) are the bottom of dominant conduction bands and the maximum of the dominant valence band. The other parameters are $M = 5\ \text{eV nm}^2$, $A = 0.5\ \text{eV nm}$, and $k_0 = 0.3\ \text{nm}^{-1}$.

The band crossing point is at $E_F = 0$. Setting $E_\pm(n, 0) = 0$, we will find that only when the magnetic field B satisfies the function

$$B_z^n = \frac{\hbar k_0^2}{2e\left(n + \frac{1}{2}\right)}, \quad n = 0, 1, 2, \ldots, \tag{9}$$

the energy gaps will be closed.

When the magnetic field is along the y direction, the vector potential is $\mathbf{A} = (Bz, 0, 0)$ under a Landau gauge. Using the Pierls transformation, the wave vector is

$$\mathbf{k} = \left(k_x + \frac{z}{\ell_B^2}, k_y, k_z\right), \tag{10}$$

and the ladder operators are

$$a = \frac{\ell_B}{\sqrt{2}}\left[k_z - i\left(k_x + \frac{z}{\ell_B^2}\right)\right], \tag{11}$$

$$a^\dagger = \frac{\ell_B}{\sqrt{2}}\left[k_z + i\left(k_x + \frac{z}{\ell_B^2}\right)\right]. \tag{12}$$

Using the ladder operator, the Hamiltonian can be written as

$$H = \begin{bmatrix} -\omega_M\left(a^\dagger a + \frac{1}{2}\right) + M_k' & \frac{A}{\sqrt{2}l_B}(a + a^\dagger) \\ \frac{A}{\sqrt{2}l_B}(a + a^\dagger) & \omega_M\left(a^\dagger a + \frac{1}{2}\right) - M_k' \end{bmatrix} \tag{13}$$

with $\omega_M = 2M/\ell_B^2$, $M_k' = M(k_0^2 - k_y^2)$.

We numerically calculate the energy bands of Landau levels using the periodic boundary condition for the magnetic field along the z direction in Fig. 2(a) and for the magnetic field along the y direction in Fig. 2(b). We choose three different magnetic fields $B = 4\ T, 5\ T$, and $8\ T$ to see the evolution of Landau bands. When the magnetic field along the z direction is $B_z^7 \approx 4\ T$ calculated using Eq. (9) with $k_0 = 0.3\ \text{nm}^{-1}$, the energy gap of Landau bands is closed as shown by the blue dashed line in Fig. 2(a). As the magnetic field is increased, the bandwidth between adjacent bands becomes wider, which can be seen from the green solid line and the red dash-dotted line in Fig. 2(a). In Fig. 2(b), when the magnetic field is along the y direction, the Landau bands show an obvious difference. There is no energy gap between the valence and conduction bands. The first Landau levels of valence and conduction bands are nearly independent of the magnetic field. These anisotropic Landau bands may result in anisotropic transport signatures, e.g., the anisotropic Hall conductivity.

For a nodal-line semimetal slab with magnetic field along the z direction, the Hamiltonian $H(k_x, k_y, k_z)$ is replaced by $H(-i\partial_x, k_y + x/\ell_B^2, -i\partial_z)$. We calculate the Landau levels using the basis $|s, \phi_i(x), \phi_n(z)\rangle = |\chi_s\rangle \otimes |\phi_i(x)\rangle \otimes |\phi_n(z)\rangle$ with [1]

$$\chi_1 = \begin{bmatrix} 1 \\ 0 \end{bmatrix}, \quad \chi_2 = \begin{bmatrix} 0 \\ 1 \end{bmatrix}, \tag{14}$$

$$\phi_i(x) = \sqrt{\frac{2}{L_x}} \sin\left[\frac{i\pi}{L_x}\left(y + \frac{L_x}{2}\right)\right], \quad n = 0, 1, 2, \ldots, \tag{15}$$

$$\phi_n(z) = \sqrt{\frac{2}{L_z}} \sin\left[\frac{n\pi}{L_z}\left(z + \frac{L_z}{2}\right)\right], \quad n = 0, 1, 2, \ldots. \tag{16}$$

It is found that $\phi_i(-L_x/2) = \phi_i(L_x/2) = 0$ and $\phi_n(-L_z/2) = \phi_n(L_z/2) = 0$ satisfy the open boundary condition. When the magnetic field is along the y direction, the Hamiltonian $H(k_x, k_y, k_z)$ is replaced by $H(k_x + z/\ell_B^2, -i\partial_y, -i\partial_z)$. We calculate the Landau levels using the same method as above.

In Fig. 3, we plot the Landau levels of a nodal-line semimetal slab under magnetic fields along the z and y direction using open boundary condition. Figures 3(a)–3(c) show the Landau levels for the magnetic field along the z direction. Figures 3(d)–3(f) show the Landau levels for the magnetic field along the y direction. Comparing Figs. 2 and 3, we can see the evolution of Landau levels from periodic boundary condition to open boundary condition. From these Landau levels with open boundary condition, we can explain the quantized sheet Hall conductivity of a nodal-line semimetal slab as

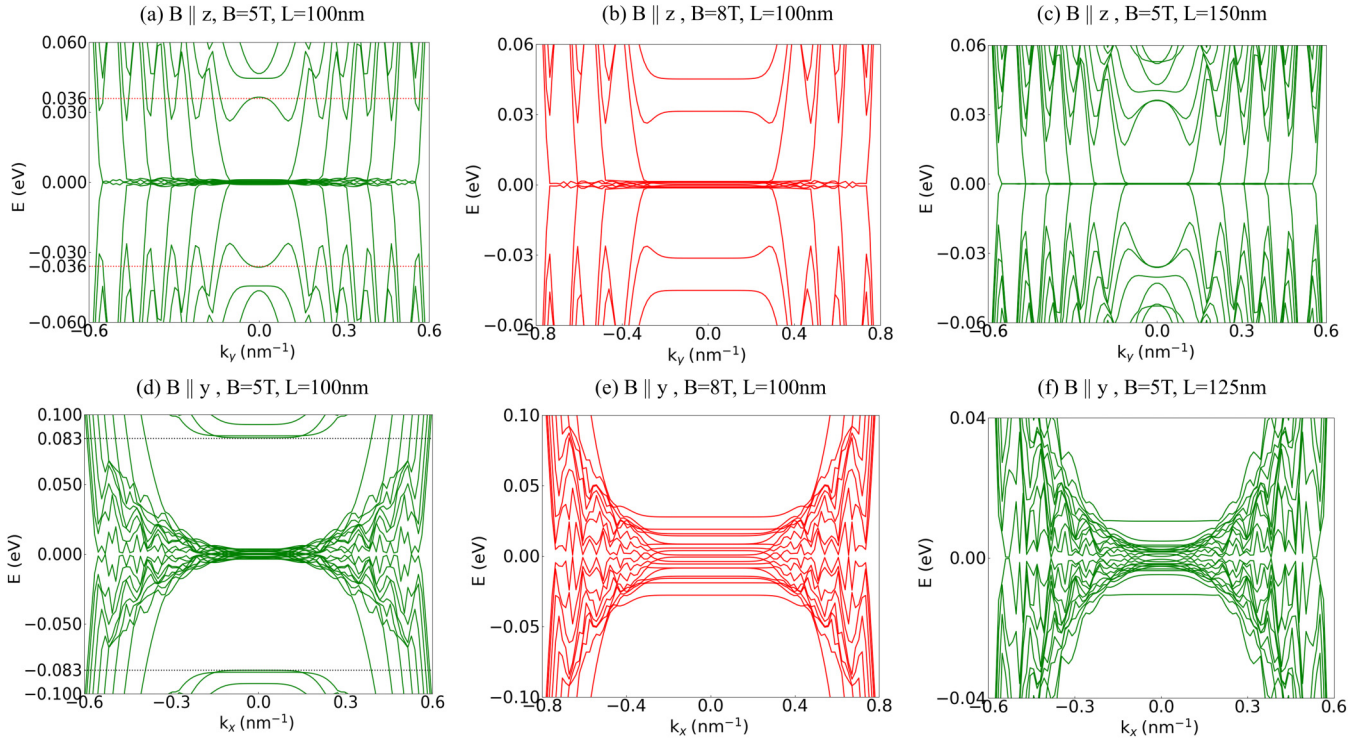

FIG. 3. The Landau level bands of a nodal-line semimetal slab with open boundary condition for (a–c) $B||z$ and (b–f) $B||y$. The magnetic fields are (a), (c), (d), (f) $B = 5\ T$ and (c), (d) $B = 8\ T$. The thicknesses along the magnetic field are (a), (b), (d), (e) $L = 100$ nm, (c) $L = 150$ nm, and (f) $L = 125$ nm. From these Landau levels, we can explain the quantized sheet Hall conductivity as shown in Figs. 4–6. Take (a) as an example: when Fermi energy is $0 < E_F < 0.036$ eV, six Landau levels cross the Fermi energy, therefore the sheet Hall conductivity is $6(e^2/h)$, which can be confirmed from Fig. 4. The other parameters are the same as in Fig. 2.

shown in Figs. 4–6. Take Fig. 3(a) as an example: when Fermi energy is $0 < E_F < 0.036$ eV, six Landau levels cross the Fermi energy, therefore the sheet Hall conductivity is $6(e^2/h)$, which can be confirmed from Fig. 4.

IV. ANISOTROPIC HALL CONDUCTIVITY

We numerically calculate the Hall conductivity of a nodal-line semimetal slab with open boundary condition in a magnetic field using the Kubo formula [1,9]

$$\sigma_{\alpha,\beta} = \frac{e^2\hbar}{iV_{\text{eff}}} \sum_{\delta,\delta'\neq\delta} \frac{\langle\Psi_\delta|v_\alpha|\Psi_{\delta'}\rangle\langle\Psi_{\delta'}|v_\beta|\Psi_\delta\rangle f_{\delta'\delta}}{(E_\delta - E_{\delta'})(E_\delta - E_{\delta'} + i\Gamma)}, \tag{17}$$

where $\alpha, \beta = x, y, z$, $|\Psi_\delta\rangle$ is the eigenstate of energy E_δ for H in a magnetic field, V_{eff} is the volume of the slab, v_α and v_β are the velocity operators, $f_{\delta'\delta} = f(E_{\delta'}) - f(E_\delta)$, and $f(x)$ is the Fermi distribution. The disorder can be introduced in the Kubo formula via the level broadening Γ. For a small Γ, the Hall conductivity can be obtained as the real part of Eq. (17).

To numerically calculate the Hall conductivity, we use the bases $|s, \upsilon, \phi_n\rangle = |\chi_s\rangle \otimes |\upsilon\rangle \otimes |\phi_n\rangle$, where $|\upsilon\rangle$ is the harmonic oscillator eigenfunction, and

$$\chi_1 = \begin{bmatrix}1\\0\end{bmatrix}, \quad \chi_2 = \begin{bmatrix}0\\1\end{bmatrix}, \tag{18}$$

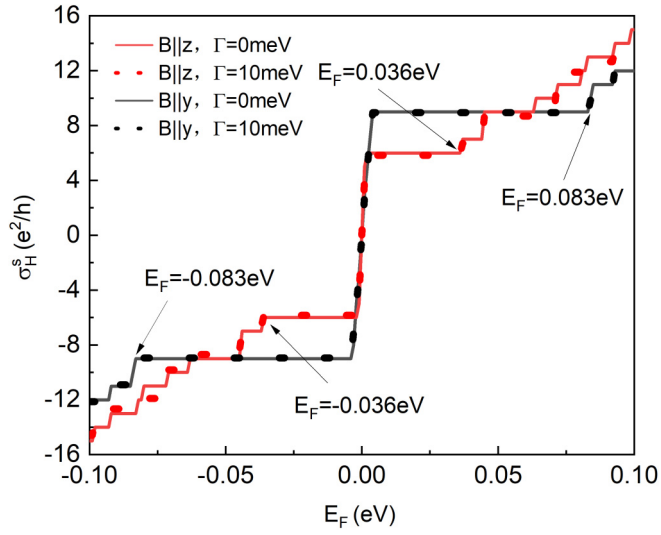

FIG. 4. In a nodal-line semimetal slab, the sheet Hall conductivity as a function of Fermi energy for $B||z$ (red line) and $B||y$ (black line) with $B = 5\ T$, $L_z = L_y = 100$ nm and $\Gamma \to 0$ (solid line), $\Gamma = 10$ meV (dotted line). The variations of the first plateau away from $E_F = 0$ are labeled in the figure. The variations of the first plateau for $B||z$ away from $E_F = 0$ are right at $E_F = \pm 0.036$ eV as the red dotted line shown in Fig. 2(a). The variations of the first plateau for $B||y$ away from $E_F = 0$ are right at $E_F = \pm 0.083$ eV as the black dotted line shown in Fig. 2(b). The other parameters are $M = 5$ eV nm^2, $A = 0.5$ eV nm, and $k_0 = 0.3$ nm^{-1}.

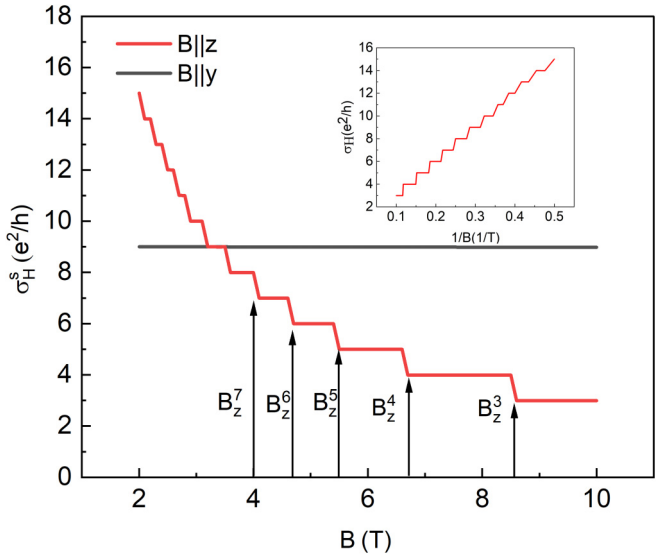

FIG. 5. The sheet Hall conductivity σ_H^s as a function of magnetic field B for $B||z$ (red line) at $E_F = 0.01$ eV, $L_z = 100$ nm and for $B||y$ (black line) at $E_F = 0.04$ eV, $L_y = 100$ nm. The inset shows the Hall conductivity as a function of $1/B$. The black arrows label the critical magnetic fields according to Eq. (9). The parameters can be found in Fig. 4

and for the magnetic field along the z direction,

$$\phi_n(z) = \sqrt{\frac{2}{L_z}} \sin\left[\frac{n\pi}{L_z}\left(z + \frac{L_z}{2}\right)\right], \quad n = 0, 1, 2, \ldots, \tag{19}$$

for the magnetic field along the y direction,

$$\phi_n(y) = \sqrt{\frac{2}{L_y}} \sin\left[\frac{n\pi}{L_y}\left(y + \frac{L_y}{2}\right)\right], \quad n = 0, 1, 2, \ldots. \tag{20}$$

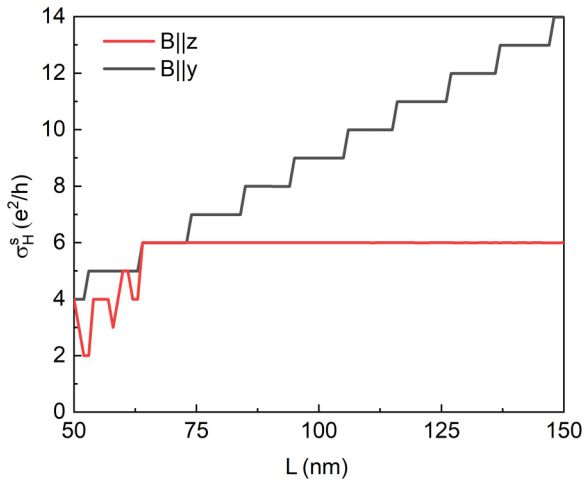

FIG. 6. The sheet Hall conductivity σ_H^s as a function of the thickness of the slab L for $B||z$ (red line) at $E_F = 0.01$ eV, $B = 5\ T$ and for $B||y$ (black line) at $E_F = 0.04$ eV, $B = 5\ T$. Here, the thickness is along the direction of the magnetic field. The parameters can be found in Fig. 4.

Apparently, $\phi_n(-L/2) = \phi_n(L/2) = 0$ satisfies the open boundary condition. Here, L is the thickness along the magnetic field. The matrix elements of the Hamiltonian (6) and (13) on the bases can be obtained as

$$H_{ss',\upsilon\upsilon',mn} = \langle s, \upsilon, \phi_m | H | s', \upsilon', \phi_n \rangle. \tag{21}$$

The eigenenergies and eigenstates of the Hamiltonian matrix can be calculated numerically and the wave function for an eigenstate of energy E_δ is

$$\Psi_\delta(x, z) = \sum_{s,\upsilon,n} C_{\delta,s\upsilon n} \varphi_\upsilon(x) \phi_n(z), \tag{22}$$

where $\{C_{\delta,s\upsilon n}\}$ are the superposition coefficients and $\varphi_\upsilon(x) = \langle x|\upsilon\rangle$.

The elements $\langle\Psi_\delta|v_x|\Psi_{\delta'}\rangle$, $\langle\Psi_\delta|v_y|\Psi_{\delta'}\rangle$, and $\langle\Psi_{\delta'}|v_z|\Psi_\delta\rangle$ in the Kubo formula can be calculated based on the velocity operators $v_x = 1/\hbar\ \partial H/\partial k_x$, $v_y = 1/\hbar\ \partial H/\partial k_y$, $v_z = 1/\hbar\ \partial H/\partial k_z$, and the wave function Ψ_δ of the energy E_δ. The sheet Hall conductivity for the nodal-line semimetal slab is defined by $\sigma_H^s = \sigma_H L$. Substituting the numerical results of the Hamiltonian matrix into the Kubo formula, we can numerically calculate the sheet Hall conductivity.

For the magnetic field along the z direction, the numerical results are calculated using Hamiltonian (6). And, the Hall conductivity σ_{xy}^H can be calculated by substituting the $\langle\Psi_\delta|v_x|\Psi_{\delta'}\rangle$ and $\langle\Psi_\delta|v_y|\Psi_{\delta'}\rangle$ into the Kubo formula. When the magnetic field is along the y direction, the Hamiltonian (13) needs to be taken into account. The Hall conductivity σ_{xz}^H can be calculated by substituting the $\langle\Psi_\delta|v_x|\Psi_{\delta'}\rangle$ and $\langle\Psi_\delta|v_z|\Psi_{\delta'}\rangle$ into the Kubo formula. For the magnetic field along the z and y directions, we numerically calculate the Hall conductivities as the functions of Fermi energy, magnetic field, and the sample thickness in Figs. 4–6, respectively. The Hall conductivity shows well-formed integer quantized plateaus.

In Fig. 4, we plot the sheet Hall conductivity as a function of Fermi energy for magnetic field $B = 5\ T$ and the thickness of the slab along the direction of the magnetic field is $L = 100$ nm. As shown in Fig. 4, the Hall conductivity is anisotropic for the magnetic field along the z and y directions. In both cases, because the energy bands in Fig. 2 for $B||z$ and $B||y$ are symmetrical with respect to $E_F = 0$, the Hall conductivities are symmetrical with respect to $E_F = 0$. The value of Hall conductivity changes dramatic when the Fermi energy is near the $E_F = 0$. As the Fermi energy changes from negative to positive, the Hall conductivity jumps from $-6e^2/h$ to $6e^2/h$ for $B||z$ and $-9e^2/h$ to $9e^2/h$ for $B||y$. The $\pm 9e^2/h$ Hall plateaus for $B||y$ are wider than $\pm 6e^2/h$ for $B||z$. In Fig. 4, we label the energies in which the first plateaus change. We also label the energies with red dotted lines in Figs. 2(a) and 3(a) and black dotted lines in Figs. 2(b) and 3(b). In Fig. 2(a), the red dotted lines are right at the bottom of conduction bands and the valence bands maximum. In Fig. 2(b), the black dotted lines cross the first Landau levels of conduction and valence bands and the bottom and top of the second Landau levels of the conduction band and valence band, respectively. According to Fig. 3, we can get the sheet Hall conductivity by counting the Landau levels of the Fermi energy crossing. From the Landau levels of a nodal-line

semimetal slab as shown in Fig. 3(a), for $B||z$, when Fermi energy is -0.036 eV $< E_F < 0.036$ eV, six Landau levels cross the Fermi energy, therefore the sheet Hall conductivity is $\pm 6e^2/h$. For $B||y$, nine Landau levels cross the Fermi energy when -0.083 eV $< E_F < 0.083$ eV. As a result, the sheet Hall conductivity is $\pm 9e^2/h$. These results are consistent with those in Fig. 4.

We also consider the effect of disorder using the same method as Ref. [1]. A finite temperature k_BT plays a similar role to the disorder. For disorder $\Gamma = 10$ meV, or equivalently, about 115 K in temperature, the Hall plateaus are stable for magnetic field along the y and z directions as shown in Fig. 4.

In Fig. 5, we plot the sheet Hall conductivity as a function of magnetic field at $E_F = 0.01$ eV for $B||z$ and at $E_F = 0.04$ eV for $B||y$. The thickness of the slab along the direction of the magnetic field is $L = 100$ nm. The features of Hall conductivity as a function of magnetic field are remarkably different for magnetic applied along the z and y directions. For the magnetic field $B||z$, the Hall conductivity follows the usual $1/B$ dependence as shown in the inset of Fig. 5. We label the B_z^n with $n = 3, 4, 5, 6, 7$ using Eq. (9) in Fig. 5. It is easy to find that the variations of plateaus are right at the B_z^n. Therefore, the plateau width in the inset of Fig. 5 can be calculated according to Eq. (9),

$$\Delta\left(\frac{1}{B}\right) = \frac{1}{B_z^n} - \frac{1}{B_z^{n-1}} = \frac{2e}{\hbar k_0^2}. \tag{23}$$

We also find that for $B_z^n < B < B_z^{n-1}$, the Hall conductivity is quantized at n (e^2/h), which can be checked from Fig. 5. However, the situation is different for $B||y$. Because the first Landau levels of the conduction band and valence band are nearly independent of the magnetic field at $E_F = 0.04$ eV, the Hall conductivity shows a straight plateau at $\sigma_H = 9(e^2/h)$ independent of the magnetic field, as shown in Fig. 5. The plateau of sheet Hall conductivity varies as the Landau levels of nodal-line semimetal change with the magnetic fields. As shown in Figs. 3(a) and 3(b), for $B||z$, six Landau levels cross $E_F = 0.01$ eV at $B = 5$ T, while four Landau levels cross $E_F = 0.01$ eV at $B = 8$ T. As a result, the sheet Hall conductivities are $\sigma_H^s = 6(e^2/h)$ at $B = 5$ T and $\sigma_H^s = 4(e^2/h)$ at $B = 8$ T, which can be confirmed in Fig. 5. For $B||y$, nine Landau levels cross $E_F = 0.04$ eV at $B = 5$ T and 8 T as shown in Figs. 3(d) and 3(e). Therefore, the sheet Hall conductivities are the same $\sigma_H^s = 9(e^2/h)$ for $B = 5$ T and 8 T in Fig. 5.

In Fig. 6, we plot the sheet Hall conductivity as a function of the sample thickness at $E_F = 0.01$ eV, $B = 5$ T for $B||z$ and at $E_F = 0.04$ eV, $B = 5$ T for $B||y$. Here, the thickness is along the direction of the applied magnetic field. The thickness-dependent Hall conductivity is also anisotropic. For $B||z$, using the parameters in Fig. 6, when the thickness $L < 64$ nm, the Hall conductivity changes drastically. When the thickness $L > 64$ nm, the Hall conductivity is shown to be independent of the thickness. For $B||y$, the Hall conductivity increases as the thickness increases. We can explain the thickness dependence of sheet Hall conductivity using a similar method. As shown in Figs. 3(a) and 3(c), for $B||z$, six Landau levels cross $E_F = 0.01$ eV for $L = 100$ nm and $L = 150$ nm. As a result, the sheet Hall conductivities are both $\sigma_H^s = 6(e^2/h)$. Therefore, the sheet Hall conductivity is shown to be independent of the thickness for $B||z$. For $B||y$, nine Landau levels cross $E_F = 0.04$ eV for $L = 100$ nm and 11 Landau levels cross $E_F = 0.04$ eV for $L = 125$ nm as shown in Figs. 3(d) and 3(f). The sheet Hall conductivities are $\sigma_H^s = 9(e^2/h)$ for $L = 100$ nm and $\sigma_H^s = 11(e^2/h)$ for $L = 125$ nm, as shown in Fig. 6. Therefore, the sheet Hall conductivity is an increasing function for $B||y$. Similar to the situation in Weyl semimetal, the sheet Hall conductivities are independent of the thickness when the magnetic field is perpendicular to the Fermi arc states, while they are an increasing function of thickness for the magnetic field parallel to the Fermi arc states. In nodal-line semimetal, the sheet Hall conductivities are also independent of the thickness for the magnetic field perpendicular to the drummer-head surface states. When the magnetic field is parallel to the drummer-head surface states, the sheet Hall conductivity is an increasing function of thickness.

V. DISCUSSION

From the results obtained above, we can discuss how the surface states influence the 3D QHE in nodal-line semimetal. As shown in Fig. 1, for the surface parallel to the nodal line, the projection of a nodal line on the surface forms a drumhead-like surface state. For the surface perpendicular to the nodal line, the projection of the nodal line is just a straight line. The anisotropic surface states give rise to the anisotropic QHE in nodal-line semimetal. For the magnetic field along the z direction, which is perpendicular to the drumhead-like surface state, it is similar to the case in Ref. [1]. The quantized sheet Hall conductivity of drumhead-like surface states shows $1/B$ dependence and independence from the thickness. On the other hand, for the magnetic field along the y direction, the QHE of the straight line surface states shows independence from the magnetic fields and increases as the thickness increase.

In Fig. 3, the Landau levels of a nodal-line semimetal slab with open boundary condition contain the information of surface states. According to Fig. 3, we can explain the sheet Hall conductivity calculated using the Kubo formula by counting the Landau levels that cross the Fermi energy. For the magnetic field along the z direction, in Figs. 3(a) and 3(b), six Landau levels cross $E_F = 0.01$ eV for $B = 5$ T, while four Landau levels cross $E_F = 0.01$ eV at $B = 8$ T. Therefore, $\sigma_H^s = 6(e^2/h)$ for $B = 5$ T and $\sigma_H^s = 4(e^2/h)$ for $B = 8$ T, consistent with the $1/B$ dependence. In Figs. 3(a) and 3(c), six Landau levels cross the Fermi energy near $E_F = 0$ for the thickness $L = 100$ nm and 150 nm, therefore the sheet Hall conductivity is $6(e^2/h)$ independent of the thickness, consistent with that in Fig. 6. As for the magnetic field along the y direction, in Figs. 3(d) and 3(e), nine Landau levels cross $E_F = 0.04$ eV for $B = 5T$ and $B = 8T$, therefore the sheet Hall conductivities are $9(e^2/h)$ independent of the magnetic field in Fig. 5. In Figs. 3(d) and 3(f), nine Landau levels cross $E_F = 0.04$ eV at $L = 100$ nm, while 11 Landau levels cross $E_F = 0.04$ eV at $L = 125$ nm, therefore the sheet Hall

conductivities are $9(e^2/h)$ for $L = 100$ nm and $11(e^2/h)$ for $L = 125$ nm, consistent with Fig. 6.

It is important to consider that some Hall plateaus originating from quantized surface states may be resistant to impurity scattering, while others stemming from bulk states may be susceptible to breakdown under such scattering. In Sec. IV, we consider the effect of disorder on the Hall plateaus via level broadening. However, the impurity effects cannot be simply attributed to level broadening. Impurity effects may also lead to level mixing or inter- and/or intravalley scattering. Therefore, it is necessary to systematically investigate the effects of impurity. Here, according to the results obtained above, we can give a qualitative analysis of the impurity effects. For the magnetic field along the z direction, the Hall conductivities are independent of the thickness. This could mean that the Hall conductivities are entirely due to the surface states. Therefore, the Hall plateaus may be resistant to impurity scattering. For the magnetic field along the y direction, the Hall conductivities are dependent on the thickness, meaning that Hall conductivities are stemming from bulk states. As a result, these Hall plateaus may be susceptible to breakdown under such scattering. A quantitative analysis of impurity effects, including bulk impurity and surface impurity, will be done in our further research.

In experiment, anomalous Hall effect [61,62] and 3D anisotropic magnetoresistance [45] have been observed in nodal-line semimetal. However, less attention has been paid to the Hall conductivity of nodal-line semimetal. We anticipate that this anisotropic QHE will be observed in nodal-line semimetal.

VI. SUMMARY

In summary, we numerically study the 3D QHE in topological nodal-line semimetals through calculating the Hall conductivity of a nodal-line semimetal. We find that the Hall conductivities are anisotropic when the magnetic fields along different directions are applied. The anisotropy of Hall conductivity manifests itself in the dependence of magnetic field, Fermi energy, and the thickness along the direction of the magnetic field. The Hall conductivity as a function of Fermi energy is symmetric with respect to $E_F = 0$. A wide quantized Hall plateau shows up when Fermi energy deviates from $E_F = 0$. The anisotropy is reflected in that the plateau of $B||y$ is bigger and wider than that for $B||z$. As for the magnetic field dependence, the Hall conductivity for $B||z$ follows the usual $1/B$ dependence. However, the Hall conductivity is independent of the magnetic field $B||y$. As for the thickness dependence, the Hall conductivity is independent of the thickness of the sample when the thickness is greater than a critical value for $B||z$. However, the Hall conductivity is an increasing function for $B||y$. We also explain this anisotropic 3D QHE from the Landau bands under magnetic fields. Our study demonstrate the anisotropic 3D QHE in nodal-line semimetal. This unique anisotropic 3D QHE can be a transport feature to recognize the nodal-line semimetals.

ACKNOWLEDGMENTS

This work was supported by the National Natural Science Foundation of China under Grant No. 12274235 (R.M.).

[1] C. M. Wang, H.-P. Sun, H.-Z. Lu, and X. C. Xie, 3D quantum Hall effect of Fermi arcs in topological semimetals, Phys. Rev. Lett. **119**, 136806 (2017).
[2] H.-Z. Lu, 3D quantum Hall effect, Nat. Sci. Rev. **6**, 208 (2019).
[3] R. Chen, T. Liu, C. M. Wang, H.-Z. Lu, and X. C. Xie, Field-tunable one-sided higher-order topological hinge states in Dirac semimetals, Phys. Rev. Lett. **127**, 066801 (2021).
[4] P. Wang, Y. Ren, F. Tang, P. Wang, T. Hou, H. Zeng, L. Zhang, and Z. Qiao, Approaching three-dimensional quantum Hall effect in bulk $HfTe_5$, Phys. Rev. B **101**, 161201(R) (2020).
[5] F. Qin, S. Li, Z. Z. Du, C. M. Wang, W. Zhang, D. Yu, H.-Z. Lu, and X. C. Xie, Theory for the charge-density-wave mechanism of 3D quantum Hall effect, Phys. Rev. Lett. **125**, 206601 (2020).
[6] H. Li, H. Liu, H. Jiang, and X. C. Xie, 3D quantum Hall effect and a global picture of edge states in Weyl semimetals, Phys. Rev. Lett. **125**, 036602 (2020).
[7] F. Tang *et al.*, Three-dimensional quantum Hall effect and metal-insulator transition in $ZrTe_5$, Nature (London) **569**, 537 (2019).
[8] R. Chen, C. M. Wang, T. Liu, H.-Z. Lu, and X. C. Xie, Quantum Hall effect originated from helical edge states in Cd_3As_2, Phys. Rev. Res. **3**, 033227 (2021).
[9] M. Chang and L. Sheng, Three-dimensional quantum Hall effect in the excitonic phase of a Weyl semimetal, Phys. Rev. B **103**, 245409 (2021).
[10] R. Ma, D. N. Sheng, and L. Sheng, Three-dimensional quantum Hall effect and magnetothermoelectric properties in Weyl semimetals, Phys. Rev. B **104**, 075425 (2021).
[11] M. Chang, H. Geng, L. Sheng, and D. Y. Xing, Three-dimensional quantum Hall effect in Weyl semimetals, Phys. Rev. B **103**, 245434 (2021).
[12] M. Chang, Y. Ge, and L. Sheng, Generalization of the theory of three-dimensional quantum Hall effect of Fermi arcs in Weyl semimetal, Chin. Phys. B **31**, 057304 (2022).
[13] X.-X. Zhang and N. Nagaosa, Anisotropic three-dimensional quantum Hall effect and magnetotransport in mesoscopic Weyl semimetals, Nano Lett. **22**, 3033 (2022).
[14] F. Xiong, C. Honerkamp, D. M. Kennes, and T. Nag, Understanding the three-dimensional quantum Hall effect in generic multi-Weyl semimetals, Phys. Rev. B **106**, 045424 (2022).
[15] M. Chang, R. Ma, and L. Sheng, Chern number and Hall conductivity in three-dimensional quantum Hall effect in Weyl semimetals, Phys. Rev. B **108**, 165416 (2023).
[16] X. Zhang, Y. Lee, V. Kakani, K. Yang, K. Cho, and X. Shi, Two types of three-dimensional quantum Hall effects in multilayer WTe_2, Phys. Rev. B **107**, 245410 (2023).
[17] X. Wan, A. M. Turner, A. Vishwanath, and S. Y. Savrasov, Topological semimetal and Fermi-arc surface states in the electronic structure of pyrochlore iridates, Phys. Rev. B **83**, 205101 (2011).

[18] A. A. Burkov and L. Balents, Weyl semimetal in a topological insulator multilayer, Phys. Rev. Lett. **107**, 127205 (2011).

[19] K. Y. Yang, Y. M. Lu, and Y. Ran, Quantum Hall effects in a Weyl semimetal: Possible application in pyrochlore iridates, Phys. Rev. B **84**, 075129 (2011).

[20] G. Xu, H. Weng, Z. Wang, X. Dai, and Z. Fang, Chern semimetal and the quantized anomalous Hall effect in $HgCr_2Se_4$, Phys. Rev. Lett. **107**, 186806 (2011).

[21] P. Delplace, J. Li, and D. Carpentier, Topological Weyl semimetal from a lattice model, Europhys. Lett. **97**, 67004 (2012).

[22] J.-H. Jiang, Tunable topological Weyl semimetal from simple-cubic lattices with staggered fluxes, Phys. Rev. A **85**, 033640 (2012).

[23] B. Singh, A. Sharma, H. Lin, M. Z. Hasan, R. Prasad, and A. Bansil, Topological electronic structure and Weyl semimetal in the $TlBiSe_2$ class of semiconductors, Phys. Rev. B **86**, 115208 (2012).

[24] J. Liu and D. Vanderbilt, Weyl semimetals from noncentrosymmetric topological insulator, Phys. Rev. B **90**, 155316 (2014).

[25] D. Bulmash, C.-X. Liu, and X.-L. Qi, Prediction of a Weyl semimetal in $Hg_{1-x-y}Cd_xMn_yTe$, Phys. Rev. B **89**, 081106(R) (2014).

[26] N. P. Armitage, E. J. Mele, and A. Vishwanath, Weyl and Dirac semimetals in three-dimensional solids, Rev. Mod. Phys. **90**, 015001 (2018).

[27] C. Zhang *et al.*, Evolution of Weyl orbit and quantum Hall effect in Dirac semimetal Cd_3As_2, Nat. Commun. **8**, 1272 (2017).

[28] C. Zhang *et al.*, Quantum Hall effect based on Weyl orbits in Cd_3As_2, Nature (London) **565**, 331 (2019).

[29] S. Nishihaya, M. Uchida, Y. Nakazawa, M. Kriener, Y. Kozuka, Y. Taguchi, and M. Kawasaki, Gate-tuned quantum Hall states in Dirac semimetal $Cd_{1-x}Zn_x)As_2$, Sci. Adv. **4**, eaar5668 (2018).

[30] M. Uchida *et al.*, Quantum Hall states observed in thin films of Dirac semimetal Cd_3As_2, Nat. Commun. **8**, 2274 (2017).

[31] T. Schumann, L. Galletti, D. A. Kealhofer, H. Kim, M. Goyal, and S. Stemmer, Observation of the quantum Hall effect in confined films of the three-dimensional Dirac semimetal Cd_3As_2, Phys. Rev. Lett. **120**, 016801 (2018).

[32] D. A. Kealhofer, L. Galletti, T. Schumann, A. Suslov, and S. Stemmer, Topological insulator state and collapse of the quantum Hall effect in a three-dimensional Dirac semimetal heterojunction, Phys. Rev. X **10**, 011050 (2020).

[33] B.-C. Lin, S. Wang, S. Wiedmann, J.-M. Lu, W.-Z. Zheng, D. Yu, and Z.-M. Liao, Observation of an odd-integer quantum Hall effect from topological surface states in Cd_3As_2, Phys. Rev. Lett. **122**, 036602 (2019).

[34] C.-K. Chiu, J. C. Y. Teo, A. P. Schnyder, and S. Ryu, Classification of topological quantum matter with symmetries, Rev. Mod. Phys. **88**, 035005 (2016).

[35] Y.-H. Chan, C.-K. Chiu, M. Y. Chou, and A. P. Schnyder, Ca_3P_2 and other topological semimetals with line nodes and drumhead surface states, Phys. Rev. B **93**, 205132 (2016).

[36] H. Weng, Y. Liang, Q. Xu, R. Yu, Z. Fang, X. Dai, and Y. Kawazoe, Topological node-line semimetal in three-dimensional graphene networks, Phys. Rev. B **92**, 045108 (2015).

[37] Y. Kim, B. J. Wieder, C. L. Kane, and A. M. Rappe, Dirac line nodes in inversion-symmetric crystals, Phys. Rev. Lett. **115**, 036806 (2015).

[38] R. Yu, H. Weng, Z. Fang, X. Dai, and X. Hu, Topological node-line semimetal and Dirac semimetal state in antiperovskite Cu_3PdN, Phys. Rev. Lett. **115**, 036807 (2015).

[39] R. Li, H. Ma, X. Cheng, S. Wang, D. Li, Z. Zhang, Y. Li, and X.-Q. Chen, Dirac node lines in pure alkali earth metals, Phys. Rev. Lett. **117**, 096401 (2016).

[40] M. Hirayama, R. Okugawa, T. Miyake, and S. Murakami, Topological Dirac nodal lines and surface charges in fcc alkaline earth metals, Nat. Commun. **8**, 14022 (2017).

[41] A. Lau and C. Ortix, Topological semimetals in the SnTe material class: Nodal lines and Weyl points, Phys. Rev. Lett. **122**, 186801 (2019).

[42] J. Hu, Z. Tang, J. Liu, X. Liu, Y. Zhu, D. Graf, K. Myhro, S. Tran, C. N. Lau, J. Wei, and Z. Mao, Evidence of topological nodal-line fermions in ZrSiSe and ZrSiTe, Phys. Rev. Lett. **117**, 016602 (2016).

[43] J. Hu, Y. L. Zhu, D. Graf, Z. J. Tang, J. Y. Liu, and Z. Q. Mao, Quantum oscillation studies of the topological semimetal candidate ZrGeM (M = S, Se, Te), Phys. Rev. B **95**, 205134 (2017).

[44] N. Kumar, K. Manna, Y. Qi, S.-C. Wu, L. Wang, B. Yan, C. Felser, and C. Shekhar, Unusual magnetotransport from Si-square nets in topological semimetal HfSiS, Phys. Rev. B **95**, 121109(R) (2017).

[45] H. Pan, B. Tong, J. Yu, J. Wang, D. Fu, S. Zhang, B. Wu, X. Wan, C. Zhang, X. Wang, and F. Song, Three-dimensional anisotropic magnetoresistance in the Dirac node-line material ZrSiSe, Sci. Rep. **8**, 9340 (2018).

[46] D. Takane, Z. Wang, S. Souma, K. Nakayama, C. X. Trang, T. Sato, T. Takahashi, and Y. Ando, Dirac-node arc in the topological line-node semimetal HfSiS, Phys. Rev. B **94**, 121108(R) (2016).

[47] A. Topp, J. M. Lippmann, A. Varykhalov, V. Duppel, B. V. Lotsch, C. R. Ast, and L. M. Schoop, Non-symmorphic band degeneracy at the Fermi level in ZrSiTe, New J. Phys. **18**, 125014 (2016).

[48] M. Neupane, I. Belopolski, M. M. Hosen, D. S. Sanchez, R. Sankar, M. Szlawska, S. Y. Xu, K. Dimitri, N. Dhakal, P. Maldonado, P. M. Oppeneer, D. Kaczorowski, F. Chou, M. Z. Hasan, and T. Durakiewicz, Observation of topological nodal fermion semimetal phase in ZrSiS, Phys. Rev. B **93**, 201104(R) (2016).

[49] L. M. Schoop, M. N. Ali, C. Straßer, A. Topp, A. Varykhalov, D. Marchenko, V. Duppel, S. S. P. Parkin, B. V. Lotsch, and C. R. Ast, Dirac cone protected by non-symmorphic symmetry and three-dimensional Dirac line node in ZrSiS, Nat. Commun. **7**, 11696 (2016).

[50] M. M. Hosen, K. Dimitri, A. Aperis, P. Maldonado, I. Belopolski, G. Dhakal, F. Kabir, C. Sims, M. Z. Hasan, D. Kaczorowski, T. Durakiewicz, P. M. Oppeneer, and M. Neupane, Observation of gapless Dirac surface states in ZrGeTe, Phys. Rev. B **97**, 121103(R) (2018).

[51] M. Mofazzel Hosen, G. Dhakal, K. Dimitri, P. Maldonado, A. Aperis, F. Kabir, C. Sims, P. Riseborough, P. M. Oppeneer, D. Kaczorowski, T. Durakiewicz, and M. Neupane, Discovery of topological nodal-line fermionic phase in a magnetic material GdSbTe, Sci. Rep. **8**, 13283 (2018).

[52] A. Yamakage, Y. Yamakawa, Y. Tanaka, and Y. Okamoto, Line-node Dirac semimetal and topological insulating phase in

noncentrosymmetric pnictides CaAgX (X = P, As), J. Phys. Soc. Jpn. **85**, 013708 (2016).

[53] T. Sato, Z. Wang, K. Nakayama, S. Souma, D. Takane, Y. Nakata, H. Iwasawa, C. Cacho, T. Kim, T. Takahashi, and Y. Ando, Observation of band crossings protected by nonsymmorphic symmetry in the layered ternary telluride Ta_3SiTe_6, Phys. Rev. B **98**, 121111(R) (2018).

[54] D. Takane, S. Souma, K. Nakayama, T. Nakamura, H. Oinuma, K. Hori, K. Horiba, H. Kumigashira, N. Kimura, T. Takahashi, and T. Sato, Observation of a Dirac nodal line in AlB_2, Phys. Rev. B **98**, 041105(R) (2018).

[55] L. S. Xie, L. M. Schoop, E. M. Seibel, Q. D. Gibson, W. Xie, and R. J. Cavaa, A new form of Ca_3P_2 with a ring of Dirac nodes, APL Mater. **3**, 083602 (2015).

[56] D. W. Zhang, Y. Q. Zhu, Y. X. Zhao, H. Yan, and S. L. Zhu, Topological quantum matter with cold atoms, Adv. Phys. **67**, 253 (2018).

[57] W. Chen, K. Luo, L. Li, and O. Zilberberg, Proposal for detecting nodal-line semimetal surface states with resonant spin-flipped reflection, Phys. Rev. Lett. **121**, 166802 (2018).

[58] W. Chen, H.-Z. Lu, and O. Zilberberg, Weak localization and antilocalization in nodal-line semimetals: Dimensionality and topological effects, Phys. Rev. Lett. **122**, 196603 (2019).

[59] R. A. Molina and J. González, Surface and 3D Quantum Hall effects from engineering of exceptional points in nodal-line semimetals, Phys. Rev. Lett. **120**, 146601 (2018).

[60] A. A. Burkov, M. D. Hook, and L. Balents, Topological nodal semimetals, Phys. Rev. B **84**, 235126 (2011).

[61] J. Cao, W. Jiang, X.-P. Li, D. Tu, J. Zhou, J. Zhou, and Y. Yao, In-Plane anomalous Hall effect in PT-symmetric antiferromagnetic materials, Phys. Rev. Lett. **130**, 166702 (2023).

[62] S. Chatterjee, J. Sau, S. Samanta, B. Ghosh, N. Kumar, M. Kumar, and K. Mandal, Nodal-line and triple point fermion induced anomalous Hall effect in the topological Heusler compound Co_2CrGa, Phys. Rev. B **107**, 125138 (2023).